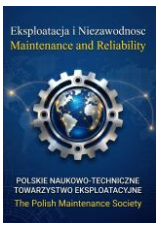

Eksploatacja i Niezawodnosc - Maintenance and Reliability

Volume 29 (2027), Issue 1

https://ein.org.pl

The Polish Maintenance Society

A surface quality analysis method for CNC milling based on an improved Z-Map algorithm

Ziling Zhang[1,*], Mengying Li[1], Baobao Qi[2,3], Zhiqiang Tao[4], Milu Zhang[1], Qiang Cheng[5]

[1] Logistics Engineering College, Shanghai Maritime University, Shanghai, 201306, China, China
[2] School of Mechanical and Aerospace Engineering, Jilin University, Changchun 130025, Jilin Province, China, China
[3] Key Laboratory of CNC Equipment Reliability, Ministry of Education, Jilin University, Changchun 130025, Jilin Province, China, China
[4] College of Robotics, Beijing Union University, Beijing, 100020, China
[5] Beijing University of Technology, Beijing 100124, China, China
* Corresponding Author: zhangziling1119@126.com

Received: 25 May 2026
Revised: 13 June 2026
Accepted: 25 June 2026
Online: 10 July 2026

Abstract

Demands for improved surface quality in high-end components have increased the need for accurate surface-quality evaluation in CNC milling. To support surface-quality analysis, this study proposes an integrated framework combining surface topography simulation, roughness prediction, and roughness reliability analysis. First, the Z-Map algorithm is enhanced using particle swarm optimization (PSO) to improve the geometric fidelity and computational robustness of three-dimensional surface topography simulation. Based on the simulation-generated data, a radial basis function neural network (RBFNN) surrogate model optimized by the improved butterfly optimization algorithm (IBOA) is established for surface roughness prediction. The proposed model achieves a coefficient of determination (R^2) of 0.9994 on the simulation-generated dataset. Furthermore, 16 independent machining experiments are conducted to evaluate the model's predictive capability under experimental conditions, achieving a Mean Absolute Percentage Error (MAPE) of 6.8%. Finally, the trained IBOA-RBFNN model is combined with Monte Carlo (MC) simulation to establish a surface roughness reliability analysis framework. The results indicate that the proposed framework maintains good agreement with experimental measurements under the investigated milling conditions and provides a feasible approach for surface-quality evaluation under the current modeling assumptions.

Keywords: *improved Z-Map algorithm, milled surface topography, IBOA-RBFNN-MC reliability model, roughness reliability*

Article citation:
Zhang Z, Li M, Qi B, Tao Z, Zhang M, Cheng Q, A surface quality analysis method for CNC milling based on an improved Z-Map algorithm, Eksploatacja i Niezawodnosc – Maintenance and Reliability 2027: 29(1) http://doi.org/10.17531/ein/225074

Highlights

- Improved Z-Map algorithm enables high-fidelity milling surface topography simulation.
- An optimized RBFNN model is proposed for surface roughness prediction.
- A roughness reliability model is proposed based on the established prediction model.
- A four-factor, four-level L_{16} orthogonal test validates the proposed method.

1. Introduction

The surface topography of mechanical components is formed through complex machining interactions and plays an important role in component performance and service life. As a key indicator of surface quality, surface roughness directly affects functional properties such as wear resistance and fatigue performance [1, 2]. Ball-nose end milling is widely used for machining complex surfaces in aerospace and other precision manufacturing fields [3]. However, the process involves highly coupled interactions between tool–workpiece engagement and machining parameters, including spindle speed, feed per tooth, and side tilt angle, which increases the difficulty of accurate surface topography simulation and surface roughness prediction. Although experimental approaches can provide direct observations, they are often time-consuming, costly, and limited in revealing the underlying surface-formation mechanisms. Under these conditions, an integrated framework combining surface topography simulation, surface roughness prediction, and roughness reliability analysis is needed to support surface-quality evaluation under complex machining conditions.

1.1. Surface topography simulation

Surface topography simulation is important for understanding the relationship between machining-process mechanics and surface quality. Existing simulation approaches can generally be classified into three categories: solid modeling methods, analytical methods, and discrete methods.

Solid modeling methods represent material removal through Boolean operations between the tool sweep volume and the workpiece. Boz et al. [4] developed tool–workpiece engagement diagrams for three-axis, five-axis, and ball-nose milling and reported that a Parasolid boundary-representation solid model provided improved computational efficiency and geometric representation compared with a dexel-field discrete model.

Analytical methods establish closed-form contact equations for surface-topography prediction. Zhang et al. [5] solved the cutting-edge trajectory using Newton iteration and achieved small geometric deviations without explicit tooth discretization. However, the convergence behavior of this method depends strongly on the initial estimates and may become unstable under complex dynamic-contact conditions.

Discrete methods, particularly the Z-Map approach, discretize the workpiece into a height grid and determine the minimum intersection height among different tool positions. Chen and Wang [6] applied a Z-Map framework to dynamic cutting-force modeling with regenerative effects, while Teimouri et al. [7] employed Z-Map for combined milling–rolling simulation. Although the conventional Z-Map method exhibits good robustness, it generally involves a trade-off between computational cost and geometric accuracy and often relies on path approximations, such as linear interpolation, which may reduce prediction accuracy for fine surface features. To improve the performance of conventional Z-Map methods, several enhanced variants have been proposed. Xu et al. [8] reduced global approximation errors by locating nodes inside swept quadrilaterals and applying local interpolation. Li et al. [9] employed Newton iteration to calculate residual heights instead of local interpolation. Xiao et al. [10] introduced a sequential quadratic programming (SQP)-based Z-Map framework to avoid explicit tool discretization. Zekalmi et al. [11] proposed several enhanced Z-Map-based algorithms (MOD1, MOD2, and MOD3) to improve the computational efficiency of surface topography simulation in 5-axis CNC milling. Guo et al. [12] combined dimension reduction with a quasi-Newton Broyden–Fletcher–Goldfarb–Shanno (BFGS) solver to improve boundary calculation in five-axis machining simulations.

Despite these developments, many existing methods still rely on simplifying approximations to improve computational efficiency. As a result, stable and accurate solution of nonlinear tool–surface intersection equations remains an important issue in surface topography simulation.

1.2. Surface roughness prediction

Predicting surface roughness is a critical step toward actively controlling the quality of milled surfaces. Existing prediction approaches can generally be classified into three categories: theoretical modeling, design-of-experiments (DOE)-based methods, and artificial-intelligence (AI)-based methods [13].

Theoretical models estimate surface roughness using tool geometry and machining kinematics. However, their prediction accuracy may decrease under practical machining conditions involving tool runout, deformation, vibration, and complex material behavior. DOE-based methods rely on experimental measurements and can provide effective predictions for specific machining conditions, but their applicability is often limited to predefined parameter ranges.

AI-based prediction methods have therefore attracted increasing attention in recent years. Salgado et al. [14] introduced a least-squares support vector machine (LSSVM) model for turning that incorporated both process and vibration features. Dyan and Hao [15] developed a PSO-LSSVM model for high-speed milling prediction. Zhao et al. [16] proposed an ensemble support vector machine (SVM) model for ceramic grinding and reported reduced mean absolute error (MAE). Xu et al. [17] constructed an adaptive neuro-fuzzy inference system (ANFIS) model combined with an improved PSO algorithm for simultaneous prediction of energy consumption and surface roughness. Neural-network-based methods have also been widely investigated. Al-Armari et al. [18] compared a backpropagation (BP) neural network with linear regression models for surface roughness prediction. Zhang et al. [19] optimized BP neural networks using genetic algorithms (GA)

and PSO for GH4169 alloy machining. Peng et al. [20] reported that radial basis function (RBF) networks exhibited improved prediction stability and convergence behavior compared with BP networks in milling applications. Zhu et al. [21] compared BP, RBF, and support vector regression (SVR) models and found that the RBF model achieved comparatively lower prediction errors. Zhan et al. [22] further enhanced surface roughness prediction for cemented carbide machining by combining three-way regression analysis with RBF networks.

Nevertheless, many existing intelligent prediction models consider only a limited number of machining parameters and do not fully account for coupled effects among process variables, such as tool radius and side tilt angle. In addition, most studies focus on planar milling conditions, whereas ball-nose milling is primarily applied to complex-surface machining.

1.3. Surface roughness reliability

Reliability analysis of surface roughness is important for evaluating the stability of surface quality under parameter uncertainty, but related studies remain relatively limited. One major difficulty arises from the highly nonlinear and implicit relationship between milling parameters and surface roughness, which complicates the construction of explicit limit-state functions. Consequently, conventional structural reliability methods, such as the first-order reliability method (FORM), the second-order reliability method (SORM), and direct MC simulation, may become computationally expensive when applied to such problems.

A common strategy is to replace implicit limit-state functions with surrogate models to improve the efficiency of reliability estimation. Representative surrogate models include polynomial response surface (PRS) models, artificial neural networks (ANNs), RBF models, SVMs, and Kriging models [23]. Deng [24] proposed three RBF-based reliability approaches, namely RBF-MCS, RBF-FORM, and RBF-SORM, for implicit limit-state problems. Wang and Fang [25] developed a tunnel reliability analysis method by integrating adaptive RBF metamodels with FORM. Abbasianjahromi and Shoiaeikhah [26] combined ANN metamodels with MC simulation to analyze the reliability of steel connections and reported improved computational efficiency compared with direct simulation. Kriging-based reliability approaches have also been extensively studied. Barbosa and Rade [27] applied Kriging metamodels with FORM to rotor–bearing systems, while Luo et al. [28] introduced an active Kriging-based conjugate FORM method (AK-CFORM) and validated it using several numerical and engineering examples. In addition, Ding et al. [29] applied SVMs to the reliability assessment of hydraulic supports and discussed their applicability to small-sample datasets. Chen et al. [30] combined SVMs with a similarity-selection strategy and a GA to develop a transient reliability method for landing-gear contact-stress analysis.

Although surrogate-based reliability methods have been widely investigated, the application of optimized RBFNN surrogate models to milling-roughness reliability analysis remains relatively limited. In particular, few studies incorporate complex parameter interactions derived from surface topography simulation into reliability analysis frameworks. Therefore, further research is still needed to integrate surface topography simulation, surface roughness prediction, and roughness reliability analysis within a unified framework.

To address the above research gaps, this study proposes an integrated framework for milled-surface-quality evaluation that combines improved Z-Map simulation, RBFNN-based roughness prediction, and roughness reliability analysis. The main contributions are summarized as follows:

1) An improved Z-Map simulation framework incorporating PSO-based nonlinear tool–workpiece intersection solving is developed for surface topography generation. Compared with interpolation-based and Newton-type approaches, the proposed framework exhibits improved convergence behavior in complex multi-solution conditions. A full-factor experimental design involving four machining parameters is further employed to generate 256 surface topography datasets for subsequent surface roughness prediction and roughness reliability analysis.
2) An IBOA-optimized RBFNN surrogate framework is established for surface roughness prediction using deterministic simulation-generated datasets. Chaotic initialization and adaptive inertia weighting are introduced to improve optimization performance. Comparative studies with Whale Optimization

Algorithm-based RBFNN (WOA-RBFNN), Pelican Optimization Algorithm-based RBFNN (POA-RBFNN), Northern Goshawk Optimization-based RBFNN (NGO-RBFNN), and standard RBFNN models are conducted to evaluate model performance under the simulation dataset.

3) A coupled IBOA-RBFNN-MC framework is developed for probabilistic roughness reliability analysis. By combining surrogate modeling with MC simulation, the proposed framework enables probabilistic sampling and analysis of the influence of machining-parameter fluctuations on surface roughness reliability.

Table 1 summarizes the differences between the proposed framework and existing methods.

Table 1. Comparison between existing methods and the proposed method.

Aspect	Existing methods	Proposed method	Key novelty
Z-Map enhancement	Newton-, SQP-, or BFGS-based gradient solvers; often relying on local linearization and initial guesses [9, 10, 12]	PSO-based tool–surface intersection solving	Derivative-free global optimization, reduced sensitivity to initial guesses, and robust convergence for strongly nonlinear and multi-modal tool–workpiece contact problems.
Roughness prediction	LSSVM, PSO-LSSVM, GA-BP, PSO-BP and standard RBFNN [14, 15, 18-22]	IBOA-optimized RBFNN	Chaotic initialization combined with fitness-adaptive inertia weighting, enabling an adaptive exploration–exploitation transition during RBFNN parameter optimization.
Reliability analysis	RBF-FORM, RBF-SORM, and Kriging-based reliability methods [24, 27, 28]	IBOA-RBFNN-MC	High-fidelity surrogate model trained on improved Z-Map data, enabling efficient MC sampling for milling surface roughness reliability evaluation.
Integration level	Typically separate modules for simulation, prediction, and reliability analysis	Fully integrated framework: Z-Map → IBOA-RBFNN → MC	End-to-end surface quality analysis chain, from high-precision topography simulation to probabilistic reliability assessment within a unified workflow.

2. Modeling the cutting edge motion trajectory

2.1. Cutting edge geometric model

Constructing an accurate geometric model of the cutting edge is important for surface topography simulation in ball-end milling. Figure 1 illustrates the helical cutting-edge geometry of a ball-end milling cutter. A tool coordinate system, denoted as O_k-$X_kY_kZ_k$, is established with the center of the tool ball as the origin, where the Z_k axis coincides with the rotational axis of the cutter.

Consider a cutting element P located on the k-th tooth, as shown in Figure 1(b). The ball-end milling cutter rotates about its axis with angular velocity ω. In the coordinate system O_k-$X_kY_kZ_k$, the coordinates of cutting element P are given by:

$$[x_p \quad y_p \quad z_p]^T = \begin{bmatrix} R\sin\varphi\cos\gamma \\ R\sin\varphi\sin\gamma \\ -R\cos\varphi \end{bmatrix} \tag{1}$$

where R is the ball-end radius of the cutter, and φ denotes the axial location angle of cutting element P. The helix lag angle γ is defined as:

$$\gamma = tan\,\beta_0\, ln\left(cot\left(\frac{\varphi}{2}\right)\right) \tag{2}$$

where β_0 is the helix angle of the cutter.

2.2. Tool edge mathematical model

To describe the trajectory of arbitrary points on the cutting edge, a kinematic model is established based on the cutter geometry. Five coordinate systems are defined, as illustrated in Figure 1(a):

(1) Workpiece-fixed coordinate system (O_l-$X_lY_lZ_l$): Serves as the reference coordinate system for tool motion and workpiece mapping.

(2) Machine spindle coordinate system (O_a-$X_aY_aZ_a$): Fixed to the spindle nose, where the Z_a axis coincides with the spindle axis and is parallel to Z_l. The X_a and Y_a axes are parallel to the machine feed directions.

(3) Tool-fixed coordinate system (O_q-$X_qY_qZ_q$): Attached to the cutter with its origin located at the ball center. This coordinate system rotates with the cutter about the Z_q axis at angular velocity ω, and the Z_q axis is collinear with Z_a.

(4) Work reference coordinate system (O_t-$X_tY_tZ_t$): Its origin coincides with O_a, and Z_t axis is parallel to Z_l. The X_t and Y_t axes represent the fixed feed directions of the machine tool and are parallel to X_l and Y_l, respectively.

(5) Tool-tip transient coordinate system (O_n-$X_nY_nZ_n$): Used to describe the local motion of a point on the k-th cutting

edge. Its origin O_n coincides with O_q, the Z_n axis is aligned with Z_q, and the coordinate system moves with the cutting point during cutter rotation.

In ball-end milling, for any point P fixed on the cutting edge, the X_n axis of the local cutting-edge coordinates system and the X_q axis of the tool coordinate system lie in the same projection plane, denoted as the $X_qO_qZ_q$ plane. Therefore, the homogeneous transformation matrix from the local cutting-edge coordinate system (O_n-$X_nY_nZ_n$) to the tool coordinate system (O_q-$X_qY_qZ_q$) is given by:

$$M_1 = \begin{bmatrix} \cos\alpha & -\sin\alpha & 0 & 0 \\ \sin\alpha & \cos\alpha & 0 & 0 \\ 0 & 0 & 1 & 0 \\ 0 & 0 & 0 & 1 \end{bmatrix} \quad (3)$$

where $\alpha = 2\pi(i-1)/k$, i denotes the tooth number, and k represents the total number of cutter teeth.

During ball-end milling, eccentricity may exist between the tool origin O_q and the spindle rotation center O_a. Meanwhile, the cutter rotates about the spindle axis Z_a. Resulting in time-varying circumferential motion of the cutting edge. Considering both tool eccentricity and spindle rotation, the transformation matrix from the tool coordinate system (O_q-$X_qY_qZ_q$) to the (O_a-$X_aY_aZ_a$) can be written as:

$$M_2 = \begin{bmatrix} \cos\rho & \sin\rho & 0 & s\cos\beta \\ -\sin\rho & \cos\rho & 0 & s\sin\beta \\ 0 & 0 & 1 & 0 \\ 0 & 0 & 0 & 1 \end{bmatrix} \quad (4)$$

where $\rho = \gamma_0 - \omega t$, γ_0 is the initial phase angle, ω is the spindle angular velocity. s is the radial projection magnitude of the tool eccentricity vector in the spindle coordinate system, β is the radial eccentricity angle, and t is the elapsed cutting time.

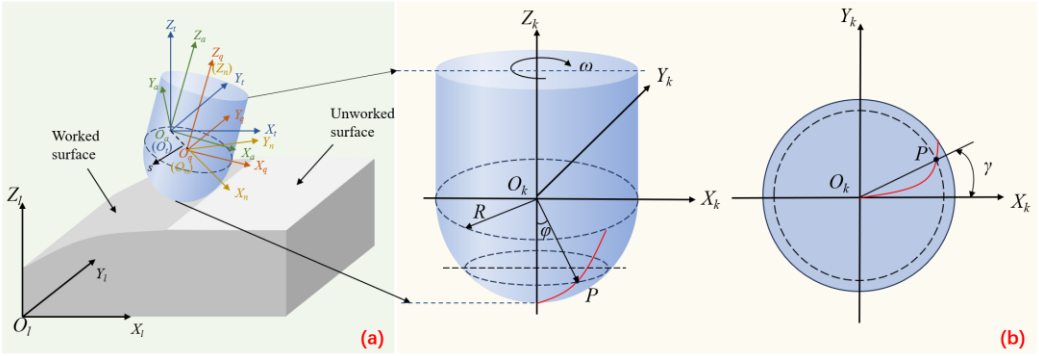

Figure 1. (a) Coordinate system for milling; (b) Cutting-edge geometry model of ball-end milling cutter.

To avoid the zero-speed cutting condition at the tool tip, the machining angle is decomposed into a side tilt angle η and a front tilt angle μ. The side tilt angle plane is η defined in the $Y_tO_tZ_t$ plane, while the front tilt μ angle is defined in the $X_tO_tZ_t$ plane. The transformation matrix from the spindle coordinate system (O_a-$X_aY_aZ_a$) to the work reference coordinate system (O_t-$X_tY_tZ_t$) is expressed as:

$$M_3 = \begin{bmatrix} 1 & 0 & 0 & 0 \\ 0 & \cos\eta & -\sin\eta & 0 \\ 0 & \sin\eta & \cos\eta & 0 \\ 0 & 0 & 0 & 1 \end{bmatrix} \cdot \begin{bmatrix} \cos\mu_0 & 0 & -\sin\mu_0 & 0 \\ 0 & 1 & 0 & 0 \\ \sin\mu_0 & 0 & \cos\mu_0 & 0 \\ 0 & 0 & 0 & 1 \end{bmatrix} \quad (5)$$

where $\mu_0 = arctan(\tan\mu\cos\eta)$.

Assuming that the translational components of the ball-center position along the x, y, and z axes are x_p, y_p, and z_p, respectively, the feed translation matrix is:

$$M_4 = \begin{bmatrix} 1 & 0 & 0 & x_p \\ 0 & 1 & 0 & y_p \\ 0 & 0 & 1 & z_p \\ 0 & 0 & 0 & 1 \end{bmatrix} \quad (6)$$

where $\begin{cases} x_p = v_f t \\ y_p = f_p N_r \\ z_p = z(i,j) \end{cases}$, v_f represents the feed speed, f_p denotes the row pitch, N_r is the current row index, and $z(i,j)$ represents the theoretical surface height at grid node. Here, i and j denote the row and column indices of the discretized workpiece grid, respectively.

Based on the above transformations, the trajectory of any point on the cutting edge in the workpiece coordinate system can be expressed as:

$$\begin{bmatrix} x_P(t,\varphi) \\ y_P(t,\varphi) \\ z_P(t,\varphi) \\ 1 \end{bmatrix} = M_4 \cdot M_3 \cdot M_2 \cdot M_1 \cdot \begin{bmatrix} x \\ y \\ z \\ 1 \end{bmatrix} \quad (7)$$

2.3. Surface topography simulation based on the improved Z-Map

Previous studies have improved the Z-Map algorithm using gradient-based optimization methods, such as Newton iteration,

SQP, and BFGS algorithms. In some studies, PSO has also been introduced for parameter calibration or auxiliary optimization tasks. However, solving the nonlinear tool–workpiece intersection equations in complex engagement regions remains challenging for conventional approaches. Gradient-based methods are sensitive to initial values and may exhibit convergence difficulties in regions with complex surface geometry.

To improve the robustness of the intersection calculation, this study incorporates a derivative-free PSO strategy into the Z-Map framework for solving the tool–workpiece intersection equations. Unlike previous studies in which PSO was mainly used for auxiliary optimization tasks, the proposed method applies PSO directly to the geometric intersection-solving process. By reducing the dependence on local linearization, the proposed approach improves the continuity of the calculated surface topography under the investigated simulation conditions. Based on the derived cutting-edge trajectory, a surface topography simulation model is established using the improved Z-Map method. The simulation process updates the residual material height by comparing the tool envelope with the discretized workpiece grid. The main simulation procedure is summarized as follows:

1. System initialization and model discretization

(1) System initialization

Initialize the cutter parameters, including the tool radius R, number of teeth N, helix angle β_0, front tilt angle μ, side tilt angle η. The machining parameters, tool path, and PSO parameters are then specified.

(2) Discretize the workpiece surface

The projection of the workpiece surface onto the $X_tO_tY_t$ plane is discretized into an $m \times n$ two-dimensional grid. The grid resolutions in the X and Ydirections are defined as: $dx = l_x/m$, $dy = l_y/n$, subject to the constraint: $max(dx, dy) \leq \frac{1}{5} min(f_z, f_p)$. Each grid node (x, y) stores an initial height value in matrix $H_z(i,j)$, where $i = 1,2,\ldots,m+1$; $j = 1,2,\ldots,n+1$ denote the row and column indices of the discretized grid, respectively. The matrix element $H_z(i,j)$ stores the discretized height value corresponding to the theoretical surface height $z(i,j)$. Figure 2(a) illustrates the milled workpiece, while Figure 2(b) presents the discretized surface mesh.

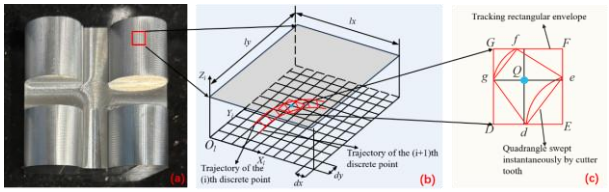

Figure 2. (a) Milling workpiece; (b) Discrete grid map of the milled workpiece; (c) tracking rectangular envelope and instantaneous swept quadrilateral diagram.

(3) Discrete cutting edges and machining time

To ensure consistency between the cutter trajectory and the discretized workpiece grid, both the machining time and cutting edge are discretized using Equations (8) and (9), respectively.

$$\Delta t = \frac{min(dx, dy)}{\omega R \sin \varphi_{max}} \tag{8}$$

$$\Delta \varphi = \frac{min(dx, dy)}{R} \tag{9}$$

the cutting time t ranges from t_{min} to t_{max}, while the axial position angle φ varies from φ_{min} to φ_{max}. Here, $\varphi_{im} = 2\arccos\left((R - a_p)/R\right)$, and $\varphi_{min} = B - 0.5\varphi_{im}$, $\varphi_{max} = B + 0.5\varphi_{im}$, where a_p denotes the axial depth of cut, $B = arccos(\cos\eta \cos\mu_0)$ denotes the tool inclination angle. If $\varphi_{min} \leq 0°$, then $\varphi_{min} = 0°$; If $\varphi_{max} \geq 90°$, then $\varphi_{max} = 90°$.

2. Rapid localization and coarse screening using the tracking rectangular envelope

The boundary coordinates of the cutting edge are calculated at the current time t and the subsequent time step $t + \Delta t$ for the angular positions φ_{min} and φ_{max}. The corresponding coordinate extrema $x_{min}, x_{max}, y_{min}$ and y_{max} are then obtained. As illustrated in Figure 2(c), the rectangular region enclosed by the four corner points $D(x_{min}, y_{min})$, $E(x_{max}, y_{min})$, $F(x_{max}, y_{max})$, and $G(x_{min}, y_{max})$ is defined as the tracking rectangular envelope. This envelope contains all workpiece grid nodes that may be swept by the cutting edge during the current motion step.

3. Precise contact detection and height value solution

(1) Construction of the swept quadrilateral and identification of valid grid nodes

Based on Step 2, the points $d\left(x(t, \varphi_{min}), y(t, \varphi_{min})\right)$, $e\left(x(t + \Delta t, \varphi_{min}), y(t + \Delta t, \varphi_{min})\right)$, $f\left(x(t + \Delta t, \varphi_{max}), y(t + \Delta t, \varphi_{max})\right)$, and $g\left(x(t, \varphi_{max}), y(t, \varphi_{max})\right)$ are connected to form the swept quadrilateral, as illustrated in Figure 2(c). Each candidate grid node $Q'(x_i, y_j)$ within the tracking rectangular envelope is then

examined. The coordinates (x_i, y_j) are tested for inclusion within the projected polygon of the swept quadrilateral in the XY-plane. If the coordinates satisfy $0 \le x_i \le l_x$ and $0 \le y_j \le l_y$, the node is considered a valid grid node within the machining region and is denoted as $Q(x_i, y_j)$, where l_x and l_y represent the workpiece dimensions in the X and Y directions, respectively. Otherwise, the current node is discarded and the next grid node is evaluated.

(2) Height-coordinate calculation

For each valid grid node $Q(x_i, y_j)$, the following nonlinear position equations between the cutter tooth trajectory and the grid node are established:

$$\begin{cases} f_x(t,\varphi) = x(t,\varphi) - x_i = 0 \\ f_y(t,\varphi) = y(t,\varphi) - y_i = 0 \end{cases} \tag{10}$$

The PSO algorithm is employed to solve Equation (10) and obtain the optimal solution pair (t', φ'). The height value of the grid node is then calculated from the cutter trajectory equation as: $z' = z(t', \varphi')$.

4. Surface topography update and result generation

(1) Verification and height update

The calculated height value z' is compared with the current stored height value $H_z(i,j)$. If the calculated value satisfies the height-update criterion, the height matrix is updated as: $H_z(i,j) = z'$. Otherwise, the original height value is retained.

(2) Iterative computation

Steps 2 and 3 are repeated for all cutter teeth within the current time step. The simulation then advances to the next time step and continues until the entire machining process is completed.

(3) Generation of surface topography and surface roughness evaluation

The final surface topography is reconstructed from the height matrix H_z. The surface roughness parameter Sa is calculated as the arithmetic mean height relative to the mean reference height:

$$Sa = \frac{1}{bc}\sum_{i=1}^{b}\sum_{j=1}^{c}|H_z(i,j) - h| \tag{11}$$

where the mean reference height h is defined as:

$$h = \frac{1}{bc}\sum_{i=1}^{b}\sum_{j=1}^{c}H_z(i,j) \tag{12}$$

here, b and c represent the number of discrete points in the X and Y directions, respectively, and $H_z(i,j)$ denotes the height value of each discrete grid node.

Regarding the PSO algorithm for solving the equation system in Step 3:

The PSO algorithm [31,32] is employed to solve the nonlinear equation system in Step 3. Gradient-based methods, such as Newton iteration, SQP, and BFGS algorithms, have been widely used in surface topography simulation. However, these methods are sensitive to initial values and may encounter convergence difficulties in regions involving complex nonlinear tool–workpiece interactions. To improve the stability of the intersection calculation, a PSO-enhanced Z-Map framework is introduced in this study. Unlike gradient-based approaches that rely on local linearization, the proposed method employs a derivative-free population-based search strategy. This approach reduces the dependence on initial-value selection and is suitable for solving nonlinear intersection equations under the investigated simulation conditions.

To qualitatively compare the solution behaviors of different methods, a representative comparison case is presented in Figure 3. In the multi-solution region shown in the figure, the gradient-based methods converge to different local solutions, resulting in discontinuities in the calculated height curve. In contrast, the PSO-based method produces a smoother height variation in the investigated case. The comparison indicates that the proposed PSO-enhanced Z-Map framework can improve the continuity and stability of the intersection calculation under complex geometric conditions.

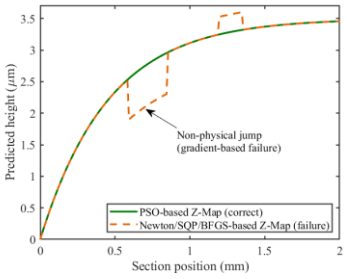

Figure 3. Failure-case comparison between the PSO-enhanced Z-Map solver and traditional gradient-based methods (Newton/SQP/BFGS).

PSO is a derivative-free, population-based optimization method in which candidate solutions, represented as particles, explore the search space. Each particle updates its velocity vector v_i and position vector q_i according to its individual best position p_i and the global best position p_g. The update equations are given as:

$$\begin{cases} v_i^d(t+1) = \omega' v_i^d(t) + a_1 r_1 \left(p_i^d(t) - q_i^d(t)\right) + a_2 r_2 \left(p_g^d(t) - q_i^d(t)\right) \\ q_i^d(t+1) = q_i^d(t) + \alpha' v_i^d(t+1) \end{cases} \tag{13}$$

where $i = 1,2,3,\dots,n$, $d = 1,2,3,\dots,D$. Here, n denotes the total number of particles, D is the search-space dimension, ω' is the inertia factor; a_1 and a_2 are acceleration coefficients, $r_1, r_2 \in [0,1]$ are uniformly distributed random numbers. The parameter α' denotes the constraint factor used to control the step size of position updating. $v_i = (v_i^1, v_i^2, \dots, v_i^D)$ and $q_i = (q_i^1, q_i^2, \dots, q_i^D)$ represent the velocity and position vectors of the i-th particle, respectively. The vectors $p_i = (p_i^1, p_i^2, \dots, p_i^D)$ and $p_g = (p_g^1, p_g^2, \dots, p_g^D)$ denote the individual best position of the particle and the global best position of the swarm, respectively.

Unlike gradient-based methods, PSO does not require derivative information and is suitable for solving nonlinear optimization problems with complex search spaces [33].

For a grid node $Q(x_i, y_i)$ within the swept quadrilateral *defg*, the corresponding tool–surface intersection should satisfy the kinematic relationship in Equation (7). Solving the nonlinear equation system is transformed into the minimization of the following objective function within the feasible domain defined by $t_{min} \le t \le t_{max}$, $\varphi_{min} \le \varphi \le \varphi_{max}$:

$$P(t,\varphi) = |x(t,\varphi) - x_i| + |y(t,\varphi) - y_i| \tag{14}$$

The PSO algorithm iteratively searches for the parameter pair (t', φ') that minimizes $P(t,\varphi)$, thereby obtaining the numerical solution of the nonlinear intersection equations. Figure 4 illustrates the simulation flowchart for the milling surface topography generation process.

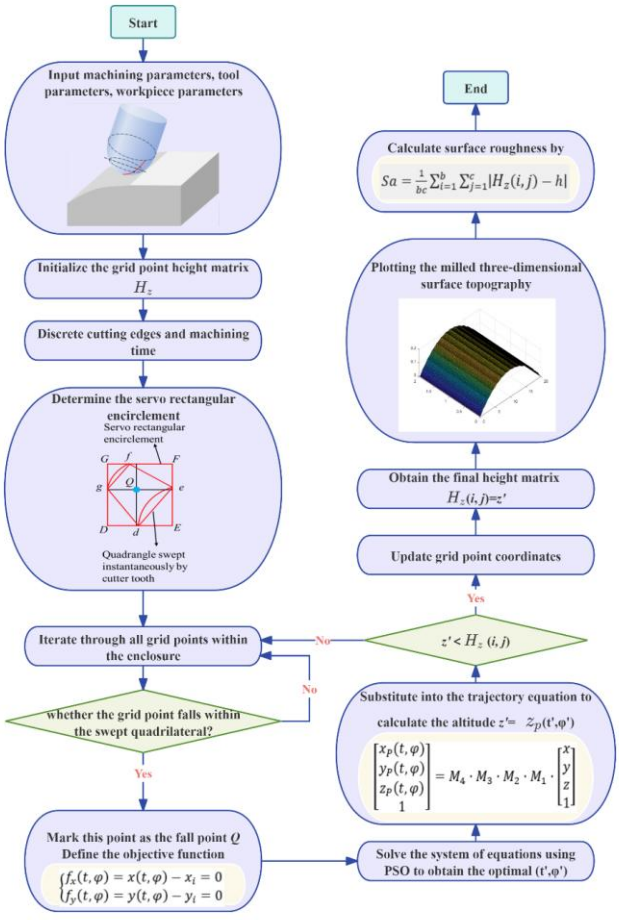

Figure 4. Flowchart of the surface topography algorithm.

3. Methodology: An IBOA-RBFNN approach for surface roughness prediction and reliability modeling

3.1. Surface roughness prediction model based on IBOA-RBFNN

Surface quality directly influences product performance, manufacturing cost, and service life. Accurate prediction of surface roughness prior to machining is essential for process parameter selection and surface quality control. However, the mapping relationship between machining parameters and surface roughness is highly nonlinear and remains complex. Therefore, an IBOA-RBFNN model is developed in this study for surface roughness prediction, and a quantitative relationship between process parameters and surface roughness is established under the investigated milling conditions.

3.1.1. RBFNN

RBFNN is a three-layer feedforward neural network composed of an input layer, a hidden layer, and an output layer. The input layer receives multidimensional feature vectors, while the hidden layer performs nonlinear transformation using radial basis functions. The output layer linearly combines hidden-layer responses to produce the final prediction. Owing to its strong nonlinear approximation capability and fast convergence, RBFNN has been widely applied in function approximation, signal processing, system modeling, and predictive control [34]. In this study, an RBFNN is adopted to construct the surface roughness prediction model, which is formulated as a single-output regression problem.

The hidden layer typically adopts the Gaussian function, which is the most commonly used radial basis function. In this study, the Gaussian function is selected as the basis function, and the hidden-layer output is expressed as:

$$G_i(x) = exp\left(-\frac{\|x - C_i\|^2}{2S^2}\right), i = 1,2,\cdots,n \qquad (15)$$

where x is the m-dimensional input vector, C_i denotes the center of the i-th radial basis function, S is the corresponding width parameter, and n represents the number of hidden neurons. The output layer performs a linear weighted summation of hidden-layer outputs. For the single-output case considered in this study, the predicted surface roughness is given by:

$$y_R = \sum_{i=1}^{n} w_i\, G_i(x) \qquad (16)$$

where w_i connection weight between the i-th hidden neuron and the output neuron.

3.1.2. IBOA

The IBOA is a nature-inspired metaheuristic that simulates butterfly foraging and mating behaviors. It performs global and local search iteratively in the solution space to identify high-quality solutions [35–39].

In the population, each butterfly generates a perceived fragrance determined by:

$$f_i = cI^{\delta} \qquad (17)$$

where f_i denotes the perceived fragrance of the i-th butterfly, c is the sensory modality, I represents the stimulus intensity, and $\delta \in [0,1]$ is a power exponent related to the search landscape.

If a butterfly detects a stronger fragrance in the search space, it moves toward the corresponding region (global search); otherwise, it performs a local search. The position update rules are defined as follows:

$$x_i^{d'+1} = x_i^{d'} + \left(r^2 x^* - x_i^{d'}\right) f_i \qquad (18)$$

$$x_i^{d'+1} = x_i^{d'} + \left(r^2 x_k^{d'} - x_j^{d'}\right) f_i \qquad (19)$$

where d' denotes the iteration index, $x_i^{d'}$ and $x_i^{d'+1}$ represent the position of the i-th butterfly at iterations $d'$and $d'+1$, respectively. x^* is the current global best solution, $x_k^{d'}$ and $x_j^{d'}$ are two randomly selected individuals from the population. $r \in [0,1]$ is a uniformly distributed random number.

The switch between global and local search is controlled by a transition probability $p \in [0,1]$. When $r < p$, global search is performed; otherwise, local search is executed.

Compared with the standard BOA, IBOA improves both population initialization and position updating strategies. First, the random initialization is replaced by an improved Tent chaotic map to enhance population diversity:

$$x_{n+1} = \begin{cases} 2x_n + 0.2\sin(rand \cdot \pi), & 0 \le x_n \le 0.5 \\ 2(1 - x_n) + 0.2\sin(rand \cdot \pi), & 0.5 < x_n \le 1 \end{cases} \qquad (20)$$

where x_n is the generated chaotic sequence value.

Second, a nonlinear adaptive inertia weight is introduced to balance exploration and exploitation dynamically:

$$w = \begin{cases} w_{min} + \dfrac{(w_{max} - w_{min})(f_i - f_{avg})}{f_{avg} - f_{min}}, & f_i \le f_{avg} \\ w_{max}, & f_i > f_{avg} \end{cases} \quad (21)$$

where w_{max} and w_{min} are upper and lower bounds of inertia weight, respectively, f_i, f_{avg} and f_{min} denote the fitness value of the i-th butterfly, the population average fitness, and the minimum fitness value, respectively. The optimization problem is treated as a minimization problem.

These improvements enhance population diversity and adaptive search capability, enabling better balance between global exploration and local exploitation, accelerating convergence, and improving robustness against local optima.

A key difference between the proposed IBOA and existing optimizers (POA, WOA, and NGO) lies in their strategies for balancing exploration and exploitation, which is essential for tuning RBFNN parameters. The POA adopts a two-phase search scheme that explicitly separates exploration and exploitation, which may reduce flexibility in complex, high-dimensional search spaces. The WOA uses a stochastic probability mechanism to control the transition between these two behaviors, which can introduce variability during optimization. The NGO is based on a prey identification-and-attack mechanism; however, its balance between exploration and exploitation is largely predefined and may be sensitive to initial conditions. In contrast, the proposed IBOA introduces two improvements to enhance search adaptability. First, an improved Tent chaotic map is used for population initialization to enhance the diversity and distribution of candidate solutions. Second, a nonlinear adaptive inertia weight strategy is introduced to adjust the search intensity according to population fitness diversity during iterations. This mechanism enables a gradual shift from exploration to exploitation as convergence proceeds. As a result, the search process becomes more stable, and the algorithm is better suited to identifying appropriate parameter configurations for the RBFNN model.

3.1.3. IBOA-optimized RBFNN prediction model

The predictive performance of the RBFNN depends on the output-layer weights, hidden-layer centers, and the Gaussian kernel width S. Among these parameters, S has a significant influence on model behavior. A smaller S a narrow Gaussian function with strong local sensitivity, whereas a larger S leads to a smoother response with a wider receptive range. Therefore, selecting an appropriate value of S is essential to balance model accuracy and generalization ability.

In this study, the IBOA is used to optimize the kernel width parameter S of the RBFNN. The optimization process searches for an optimal value of S that minimizes training error while maintaining acceptable generalization performance. After optimization, the final IBOA-RBFNN model is constructed for surface roughness prediction.

3.2. Roughness reliability model based on IBOA-RBFNN

The surface topography model presented earlier indicates that surface roughness is strongly affected by process parameters such as feed per tooth, pitch, tool radius, and side tilt angle. In CNC milling, small variations in these parameters may lead to noticeable changes in surface roughness, thereby affecting the final surface quality. Reliability analysis is therefore introduced to characterize the uncertainty of surface roughness and to quantify the probability of surface roughness exceeding a specified limit under parameter uncertainty, thereby supporting quality risk assessment in machining processes.

The relationship between surface roughness and the above process parameters is nonlinear and implicit, making it difficult to express in closed form. For such problems, reliability analysis methods such as MC simulation, response surface methods, and surrogate modeling are commonly used. However, direct MC simulation is computationally expensive due to the large number of required samples, while response surface methods may exhibit reduced accuracy when handling strong nonlinearities. Surrogate modeling provides an alternative approach for approximating the performance function.

In this study, an IBOA-RBFNN-based MC framework is developed for roughness reliability analysis. The RBFNN is used to approximate the nonlinear mapping between process parameters and surface roughness. The simulation model described in Section 2 is used to generate training data for the network. After training, the RBFNN serves as a surrogate model for evaluating the limit state function. Based on MC simulation, a large number of samples are efficiently evaluated using the trained surrogate model, enabling reliability estimation of surface roughness. The overall procedure of the IBOA-RBFNN-MC reliability model is summarized as follows.:

(1) A training dataset is generated using the CNC milling surface topography simulation model: $D = \{u_i, y(u_i) | i = 1,2,\dots,N\}$, where $u = [f_z, f_p, R, \eta]$ denotes the vector of random machining parameters, and $y(u_i)$ represents the surface roughness response under different realizations of the input variables.

(2) The IBOA-RBFNN model is trained using the generated dataset.

(3) A probabilistic model is defined for the input variables, and MC samples are generated accordingly. In this study, the machining parameters are assumed to follow independent normal distributions $N(\mu, \sigma^2)$, where μ is the nominal value and σ represents manufacturing variability. This assumption provides a practical approximation for reliability analysis under stable machining conditions. However, real machining processes may exhibit bounded, skewed, multimodal, or correlated variations due to tool wear, machine-tool vibrations, and fixture conditions, which may influence tail probability estimation of surface roughness failure. Based on typical machining tolerances, the standard deviations are defined as follows: feed per tooth $\sigma_{f_z} = 0.05\text{mm/z}$, row pitch $\sigma_{f_p} = 0.1$ mm, tool radius $\sigma_R = 0.5$ mm, and side tilt angle $\sigma_\eta = 5°$. A total of M MC samples are generated to form the sample set $\{u_i\}_{i=1}^{M}$, where u_i denotes the machining input vector defined previously

(4) The MC samples are propagated through the trained IBOA-RBFNN model to evaluate the performance function $G(u)$.

$$G(u) = Sa_{lim} - g(u) \tag{22}$$

where Sa_{lim} denotes the allowable maximum roughness, and $g(u)$ is the roughness predicted by the IBOA-RBFNN model. The system is considered to be in the failure domain when $G(u) \leq 0$, and in the safe domain $G(u) > 0$.

(5) The number of failure samples N is counted, and the failure probability is estimated using the MC-based surrogate model:

$$P_f = P(G(u) \leq 0) = \frac{1}{M}\sum_{i=1}^{M} I\left(G(u_i)\right) = \frac{N}{M} \tag{23}$$

where M denotes the total number of MC samples , and $I\left(G(u_i)\right)$ represents the zero-one indicator function mathematically defined as:

$$I\left(G(u_i)\right) = \begin{cases} 1, G(u_i) \leq 0 \\ 0, G(u_i) > 0 \end{cases} \tag{24}$$

In summary, the procedure for roughness reliability evaluation using the IBOA-RBFNN-MC framework is illustrated in Figure 5.

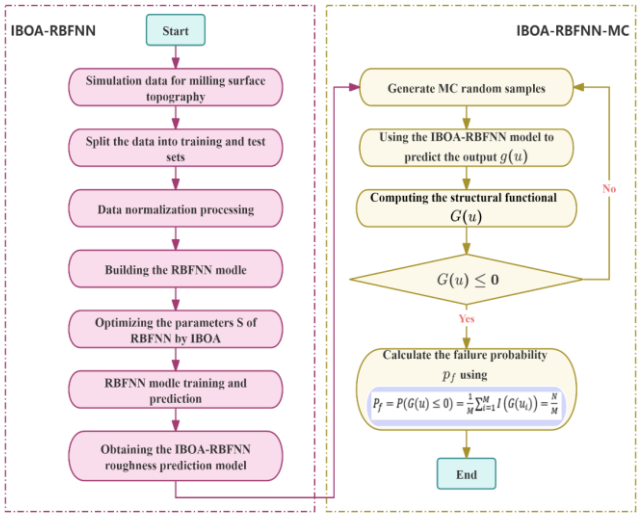

Figure 5. Flowchart of surface roughness reliability modeling based on IBOA-RBFNN-MC.

4. Analysis of model results

4.1. Efficiency analysis of the improved Z-Map algorithm

To evaluate computational efficiency, the average runtime per surface simulation was compared between the conventional Z-Map algorithm and the proposed PSO-enhanced version. For a representative 200×200 discretized surface, the conventional Z-Map requires 47 s per simulation, while the PSO-enhanced Z-Map requires approximately 123 s, corresponding to an increase of about 2.6 times in computational cost.

To assess this trade-off, an accuracy–efficiency comparison was conducted. As summarized in Table 9, the conventional Z-Map yields a profile-level root mean squared error (RMSE) of 0.0044–0.0146 μm, whereas the PSO-enhanced Z-Map reduces this value to 0.0020–0.0055 μm under the same evaluation profiles, corresponding to an average reduction of approximately 62%. This improvement helps reduce staircase artifacts and better preserves cutter–workpiece interaction details, which are important for representing complex surface

geometries.

It should be noted that the additional computational cost is incurred only during offline data generation. Discretization errors in surface reconstruction may propagate through the surrogate modeling process and influence the estimation of failure probabilities. Therefore, improving the fidelity of the generated surface data helps provide a more consistent training dataset for surrogate modeling, which is beneficial for reliability analysis. In addition, since height evaluations at different grid nodes are independent at the computational level, the method is suitable for parallel implementation on multi-core CPU or GPU architectures, which may further improve computational efficiency.

Finally, the simulated surface topography data generated by the improved Z-Map algorithm are used to train and evaluate the proposed IBOA-RBFNN model. The prediction performance and comparative results are presented in the following subsection.

4.2. Prediction performance and comparative analysis of IBOA-RBFNN

Building upon the validated efficiency of the improved Z-Map simulation framework, this subsection evaluates the prediction performance of the IBOA-RBFNN model trained using the generated surface topography data.

The model is trained and evaluated using a dataset of 256 samples generated from a full-factorial design (four parameters at four levels, 4^4=256). The corresponding parameter ranges are listed in Table 3, while the simulated surface roughness results obtained from the improved Z-Map model are provided in Table 4. This design provides a structured sampling strategy over the defined parameter space and captures nonlinear interactions among machining variables.

The use of a 4^4=256 full-factorial design for simulation-based learning has been widely adopted in similar studies. For instance, Gotkhindikar et al. [40] used the same design for training a deep neural network in additive manufacturing applications. Jiang and Gu [41] applied it in crashworthiness optimization using a back-propagation neural network. Freites et al. [42] also employed a four-level full factorial design for machine learning-based reservoir characterization. These studies indicate that such a design is commonly used in simulation-driven machine learning problems across engineering applications.

It should be noted that the dataset is entirely generated from the improved Z-Map simulation, which produces deterministic outputs without experimental noise. Therefore, the reported performance metrics reflect the model's ability to approximate the simulation-based mapping rather than experimental measurements. An 85%–15% training–testing split (218 training samples and 38 testing samples) is adopted, which is a commonly used strategy for datasets of this size [43], providing a balance between model training and independent evaluation.

To ensure a fair comparison, all models were evaluated under identical data preprocessing procedures and using the same training/testing split. The RBFNN architecture, including the number of hidden neurons and stopping criteria, was kept consistent across all methods. For optimization-based models, population size and maximum number of iterations were also fixed. In addition, 30 independent runs were conducted for all stochastic algorithms under identical settings.Therefore, the observed performance differences mainly reflect the effectiveness of the respective optimization strategies in determining the RBFNN parameters. The detailed parameter settings used for the comparative study are summarized in Table 2.

Table 2. Parameter settings for comparative models.

Configuration Parameter	IBOA-RBFNN	WOA-RBFNN	POA-RBFNN	NGO-RBFNN	RBFNN
Training/testing split	85%/15%	85%/15%	85%/15%	85%/15%	85%/15%
Hidden neurons	10	10	10	10	10
Population size	30	30	30	30	N/A
Maximum iterations	50	50	50	50	N/A
Independent runs	30	30	30	30	N/A

Table 3. Different input parameter values.

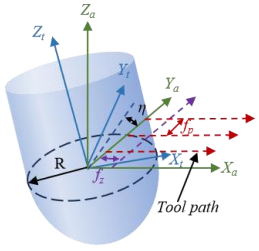

Input parameters	Input value
Feed per tooth (f_z, mm/z)	0.2, 0.3, 0.4, 0.5
Row pitch (f_p, mm)	0.2, 0.4, 0.6, 0.8
Tool radius (R, mm)	3, 4, 5, 6
Side tilt angle (η, °)	0, 10, 20, 30

Table 4. Simulated surface roughness values for different parameters.

Feed per tooth (mm/z)	Row pitch (mm)	Tool radius (mm)	Side tilt angle (°)	Surface Roughness (μm)
0.2	0.2	3	0	1.0398
0.2	0.4	3	0	1.9853
0.2	0.6	3	0	3.6620
0.2	0.8	3	0	6.6311
0.3	0.2	3	0	1.2145
0.3	0.4	3	0	3.1417
0.3	0.6	3	0	4.4875
⋮	⋮	⋮	⋮	⋮
0.3	0.2	5	10	0.6754
0.4	0.4	5	20	1.4204
0.5	0.6	5	30	2.6664
0.2	0.2	6	0	0.5315
0.3	0.4	6	10	0.9238
0.4	0.6	6	20	1.9450
0.5	0.8	6	30	3.4887

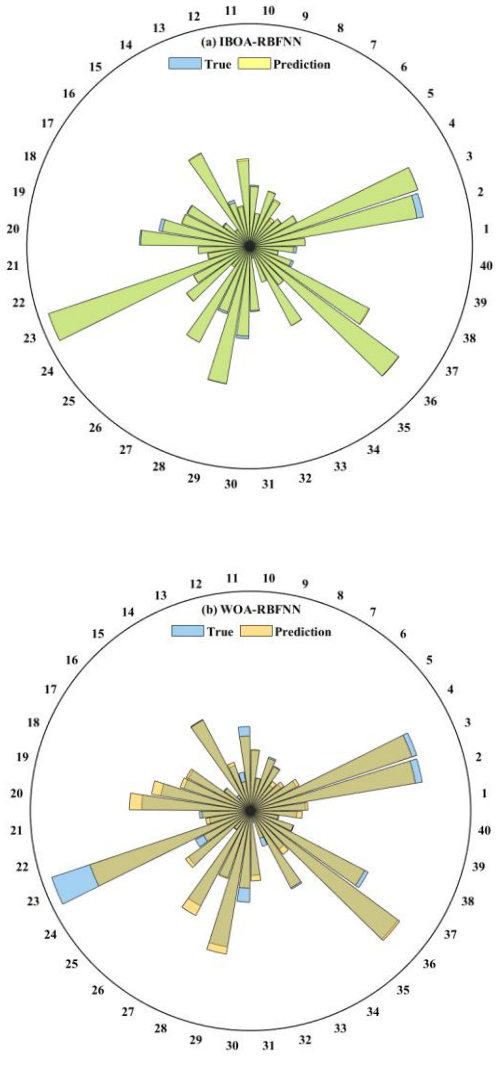

Figure 6. Comparison of actual and predicted values for different prediction models: (a) IBOA-RBFNN; (b) WOA-RBFNN; (c) POA-RBFNN; (d) NGO-RBFNN; (e) RBFNN.

Figure 6(a) illustrates the prediction results of the IBOA-RBFNN model using a circular sector plot, where blue and yellow sectors represent the actual and predicted surface roughness values, respectively. The close agreement in radial lengths indicates that the model can capture variations in surface roughness with good accuracy.

This study compares the IBOA-RBFNN model with several benchmark models, including WOA-RBFNN, POA-RBFNN, NGO-RBFNN, and standard RBFNN, using the same dataset and identical settings for all models. The comparison between predicted and actual values is shown in Figures 6(b)–(e). Quantitative error distributions are presented in Figure 7, where Figure 7(a) shows the MAE histogram and Figure 7(b) presents the relative error (RE) box plot. The IBOA-RBFNN model yields the lowest MAE (approximately 0.0428) and exhibits smaller dispersion in RE compared with the other models, indicating more stable prediction performance within the simulation-based dataset.

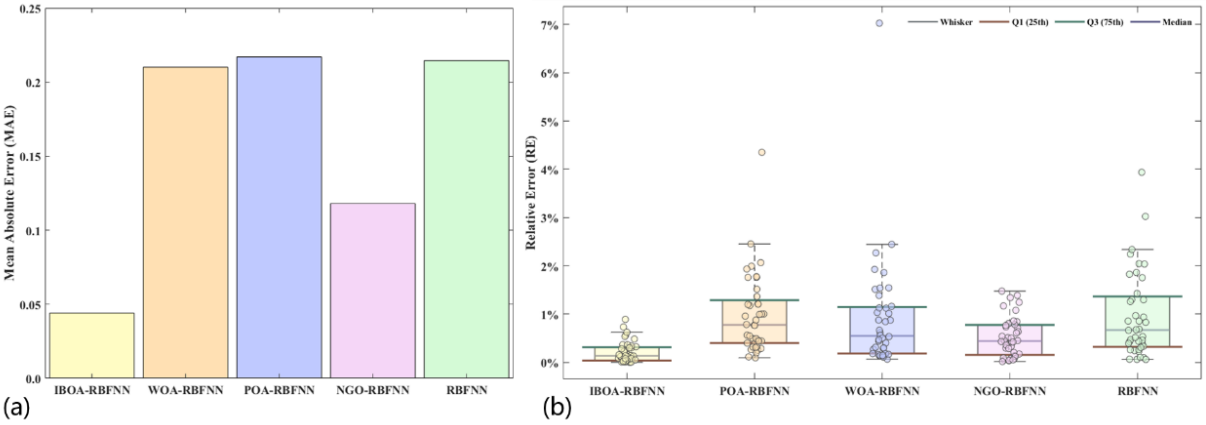

Figure 7. (a) Distribution diagrams of mean absolute error for different prediction models; (b) Distribution diagrams of relative errors for different prediction models.

Multiple evaluation metrics, including mean squared error (MSE), MAE, RMSE, MAPE, and R^2, are summarized in Table 5. The IBOA-RBFNN model achieves an RMSE of 0.0648, an MAE of 0.0428, and an R^2 of 0.9994, showing improved predictive performance compared with the standard RBFNN model. The relatively high R^2 value is attributed to the deterministic nature of the simulation-generated dataset, which provides a noise-free mapping between input variables and output responses. Therefore, these results reflect the model's ability to approximate the simulation-based relationship rather than experimental measurements. Compared with other optimization-based RBFNN models, the proposed IBOA improves prediction accuracy and reduces error variability across evaluation metrics.

The expressions for the evaluation metrics are given as follows:

$$MAE = \frac{1}{n}\sum_{i=1}^{n}|\hat{y}_i - y_i| \tag{25}$$

$$MSE = \frac{1}{n}\sum_{i=1}^{n}(y_i - \hat{y}_i)^2 \tag{26}$$

$$RMSE = \sqrt{\frac{1}{n}\sum_{i=1}^{n}(y_i - \hat{y}_i)^2} \tag{27}$$

$$R^2 = 1 - \frac{\sum_{i=1}^{n}(y_i - \hat{y}_i)^2}{\sum_{i=1}^{n}(y_i - \bar{y})^2} \tag{28}$$

$$MAPE = \frac{1}{n}\sum_{i=1}^{n}\left|\frac{\hat{y}_i - y_i}{y_i}\right| \tag{29}$$

where n denotes the number of samples; y_i is the actual surface roughness value, $\hat{y}_i$ is the predicted value, and $\bar{y}$ is the mean of the actual values.

Table 5. Performance evaluation metrics of various prediction models.

Index / Method	MAE	MSE	RMSE	R^2	MAPE	Total runtime (s)
IBOA-RBFNN	0.0428	0.0042	0.0648	0.9994	0.0171	8.5
POA-RBFNN	0.2160	0.0083	0.0911	0.9965	0.0864	7.1
WOA-RBFNN	0.2201	0.0100	0.1000	0.9880	0.0880	9.8
NGO-RBFNN	0.1213	0.1354	0.3680	0.9836	0.0485	6.3
RBFNN	0.2135	0.1127	0.3357	0.9801	0.0884	4.5

To quantitatively compare the computational cost of different optimizers during RBFNN training, the runtime was recorded on the same computing platform. IBOA, POA, WOA,

and NGO were all configured with a population size of 30 and a maximum of 50 iterations. As shown in Table 5, IBOA exhibits a moderate increase in computational cost compared with POA and NGO, with an overhead of approximately 20–35%, while remaining more efficient than WOA. This additional cost is offset by the improvement in prediction accuracy. The results suggest that, through chaotic initialization and an adaptive inertia weight strategy, IBOA achieves a more effective exploration–exploitation balance, leading to improved parameter selection for the RBFNN model under an acceptable computational budget.

The relatively high performance metrics reported in Table 5 (for example, R^2 = 0.9994, RMSE=0.0648) mainly reflect the surrogate model's ability to reproduce the deterministic relationships embedded in the improved Z-Map simulation. These results represent model fidelity to the simulation environment rather than predictive accuracy under real machining conditions. In practical milling processes, additional uncertainties such as tool wear, vibration, thermal effects, and material variability may introduce deviations that are not explicitly included in the current deterministic framework. Therefore, the differences between simulation-based results and experimental validation results can be expected and reflect the gap between idealized modeling assumptions and real machining environments.

4.3. Quantitative analysis of IBOA optimization performance

Compared with meta-heuristic optimizers commonly used for RBFNN parameter tuning, such as POA, WOA, and NGO, these methods may suffer from premature convergence and limited exploration–exploitation adaptability when handling the coupled parameter space of surface roughness prediction. In contrast, the proposed IBOA-RBFNN framework introduces two main improvements: (1) an improved Tent chaotic map to enhance population diversity during initialization, and (2) a nonlinear adaptive inertia weight strategy to adjust the search intensity based on population fitness diversity.

To quantitatively evaluate the optimization performance, a comparison with POA, WOA, and NGO was conducted under identical settings, including a population size of 30, a maximum of 50 iterations, and 30 independent runs. All algorithms were used to optimize the RBFNN width parameter, with MSE on the validation set as the fitness function. The results are summarized in Table 6.

Table 6. Quantitative comparison of optimization performance for RBFNN parameter tuning.

Algorithm	Best fitness (MSE)	Mean fitness (MSE)	Standard deviation	Average convergence iteration	Average runtime (s)
IBOA	0.000842	0.000987	0.000108	15.3	8.5
POA	0.00215	0.00342	0.000673	23.8	7.1
WOA	0.00376	0.00513	0.000894	31.5	9.8
NGO	0.00298	0.00428	0.000756	28.2	6.3

Note: Fitness values refer to the MSE of the RBFNN on the validation set during optimization. Convergence is defined as reaching a fitness value below 10^{-2}. Results are averaged over 30 independent runs.

Under identical optimization settings and network structures, IBOA achieves the lowest best fitness (0.000842) and mean fitness (0.000987), indicating improved optimization performance. In addition, IBOA shows a lower standard deviation (0.000108) compared with POA (0.000673), WOA (0.000894), and NGO (0.000756), suggesting more stable results across independent runs.

Regarding convergence behavior, IBOA reaches the predefined threshold (fitness < 10^{-2}) in an average of 15.3 iterations, which is lower than POA (23.8 iterations) and WOA (31.5 iterations). This improvement can be attributed to the enhanced initialization diversity and adaptive adjustment of search intensity during iteration.

In terms of computational cost, IBOA requires a slightly higher average runtime (8.5 s) than POA (7.1 s) and NGO (6.3 s), mainly due to additional computations in the adaptive mechanism. However, it remains more efficient than WOA (9.8 s). The additional cost relative to POA and NGO (approximately 20–35%) is offset by improvements in optimization accuracy and convergence efficiency.

These results indicate that the proposed IBOA provides improved optimization performance and stability for RBFNN parameter tuning. The faster convergence and more consistent search behavior contribute to the improved prediction accuracy of the IBOA-RBFNN model presented in Section 4.2.

4.4. Model robustness validation

Beyond the predictive performance reported in Section 4.2, the stability and generalization capability of the proposed IBOA-RBFNN model were further evaluated to address potential

overfitting concerns.

To ensure reliable assessment, several validation strategies were employed. The dataset was generated using a full-factorial design, forming a structured sampling grid in the four-dimensional parameter space defined by f_z, f_p, R, and η. The training and test sets were constructed using non-overlapping parameter combinations. Although both subsets originate from the same predefined parameter domain, the model was evaluated on unseen combinations, enabling assessment of its interpolation capability within the simulation space.

To reduce model complexity, a relatively simple RBFNN architecture was adopted. The dataset was split into training (85%) and testing (15%) sets prior to model training, and the test set was kept independent throughout the optimization process. Early stopping was also applied during training to limit potential overfitting.

In addition, a 5-fold cross-validation procedure was conducted to further assess robustness. In each fold, the model was trained on 80% of the data and validated on the remaining 20%. As summarized in Table 7, the model shows consistent performance across all folds, with relatively small variations in evaluation metrics, indicating stable behavior under different data partitions.

Table 7. 5-fold cross-validation results of the IBOA-RBFNN model.

Fold	MAE	MSE	RMSE	R^2	MAPE
1	0.0445	0.0043	0.0656	0.9993	0.0178
2	0.0430	0.0040	0.0632	0.9995	0.0172
3	0.0458	0.0048	0.0693	0.9992	0.0183
4	0.0420	0.0038	0.0616	0.9996	0.0168
5	0.0442	0.0045	0.0671	0.9994	0.0177
Mean ± Std	0.0439 ± 0.0014	0.0043 ±0.0004	0.0654 ± 0.0029	0.9994 ± 0.0002	0.0176 ± 0.0005

It should be noted that the proposed model achieves high prediction accuracy on the simulation-generated dataset. However, since the training data are derived from deterministic Z-Map simulations under controlled conditions, the cross-validation results primarily reflect interpolation performance within the predefined parameter space. To further evaluate practical generalization capability, independent experimental validation under real machining conditions is presented in Section 5.2.

5. Experimental validation

5.1. Experimental validation of surface roughness and topography

An orthogonal experimental design was adopted to validate the relationship between surface roughness and surface topography. Based on the selected factors and levels, four process parameters were investigated, each at four levels, resulting in 16 experimental runs arranged using an L_{16} orthogonal design. The factor levels are summarized in Table 8.

Table 8. Milling orthogonal experiment parameter schemes.

NO.	Feed per tooth(mm/z)	Row pitch (mm)	Tool radius (mm)	Side tilt angle(°)
1#	0.2	0.2	3	0
2#	0.3	0.4	3	10
3#	0.4	0.6	3	20
4#	0.5	0.8	3	30
5#	0.3	0.2	4	20
6#	0.4	0.4	4	30
7#	0.5	0.6	4	0
8#	0.2	0.8	4	10
9#	0.4	0.2	5	30
10#	0.5	0.4	5	20
11#	0.2	0.6	5	10
12#	0.3	0.8	5	0
13#	0.5	0.2	6	10
14#	0.2	0.4	6	0
15#	0.3	0.6	6	30
16#	0.4	0.8	6	20

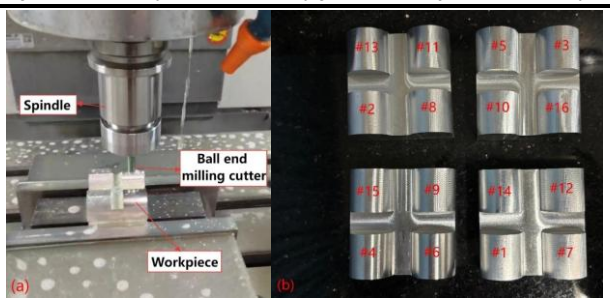

Figure 8. Milling process and milled workpieces under different parameter settings: (a) Milling process; (b) Semicylindrical surface workpieces machined with different parameters.

The experiments were conducted on a four-axis CNC machine tool. The workpiece material was 7050 aluminum alloy, and a double-flute end mill with a 30° helix angle and 50 mm tool length was used. It should be noted that the experimental validation is conducted under specific milling conditions, including a fixed workpiece material, tool geometry, and parameter range. Therefore, the purpose of this section is to evaluate the effectiveness of the proposed framework within the investigated machining configuration. Further validation under broader machining conditions and different manufacturing environments will be considered in future work to assess the generalizability of the proposed method.

The experimental setup is illustrated in Figure 8, where Figure 8(a) shows the machining process and Figure 8(b) shows the finished workpieces. Each specimen is labeled according to the experimental plan defined in Table 8.

Surface measurements were performed using a profilometer (Figure 9), with a maximum horizontal range of 100 mm, vertical range of 80 mm, and a resolution of 0.01–10 μm. The measurement regions were predefined for each specimen, and surface profiles were obtained by sequential scanning. The surface roughness values were then calculated according to Equation (11).

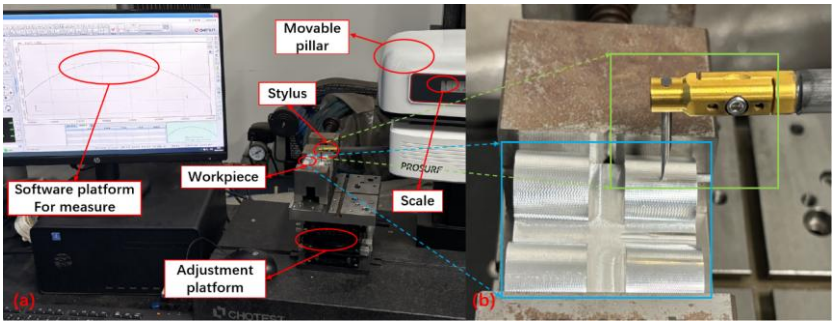

Figure 9. Surface profile measuring instrument.

Figure 10 compares the simulated and experimentally measured surface roughness under different machining conditions. The experimental results are represented by black dashed lines, while the improved Z-Map and conventional Z-Map predictions are shown using blue and pink markers, respectively. As shown in Figure 10(a), the improved Z-Map model exhibits better agreement with experimental measurements compared with the conventional method. The relative error is generally within 10%, indicating improved predictive consistency under the investigated machining conditions.

To further evaluate the consistency between simulation results and experimental measurements, four representative cases were selected from the test set. Two-dimensional surface profiles along the feed direction were extracted and compared between the improved Z-Map model, the conventional Z-Map model, and experimental measurements.

The RMSE and MAPE metrics were used to quantify the differences between simulation and experimental results. The corresponding definitions are given as follows:

$$RMSE = \sqrt{\frac{\sum_{i=1}^{m}\left(h(x_i,y_j) - h(X_i,Y_j)\right)^2}{m}} \tag{30}$$

$$MAPE = \frac{1}{m}\sum_{i=1}^{m}\left|\frac{h(x_i,y_j) - h(X_i,Y_j)}{h(X_i,Y_j)}\right| \tag{31}$$

where m denotes the number of measurement points, $h(x_i,y_j)$ represents the simulated profile height, and $h(X_i,Y_j)$ denotes the experimentally measured profile height. (x_i,y_j) and (X_i,Y_j) refer to the spatial coordinates of the simulation grid and the experimental measurement points, respectively.

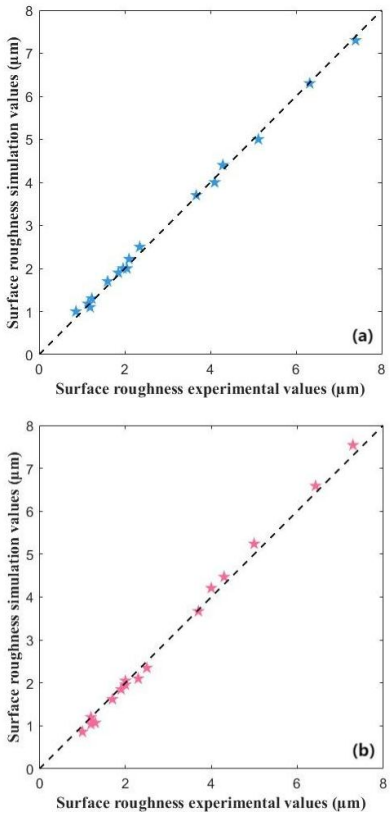

Figure 10. Comparison chart of surface roughness simulation and experimental Results: (a) PSO-enhanced Z-Map algorithm; (b) Conventional Z-Map algorithm.

Figures 11(a)–(d) show the 2D profile comparisons for

parameter sets 2, 6, 11, and 13. In all cases, the improved Z-Map results (blue curves) show better agreement with experimental profiles (red curves) compared with the conventional Z-Map results (black curves). The corresponding 3D surface renderings further illustrate the differences between the two simulation methods. The maximum residual heights for the four cases are 0.201, 0.195, 0.212, and 0.192 μm, respectively, showing similar trends between simulation and experimental results.

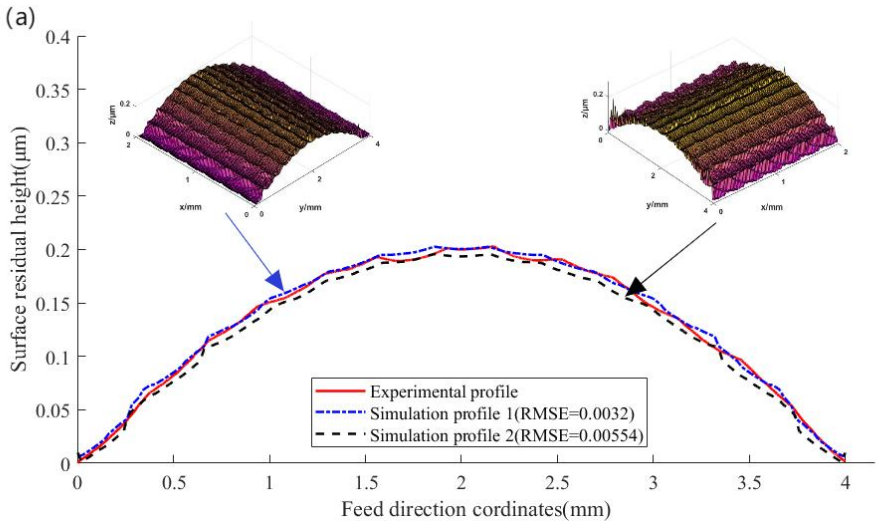

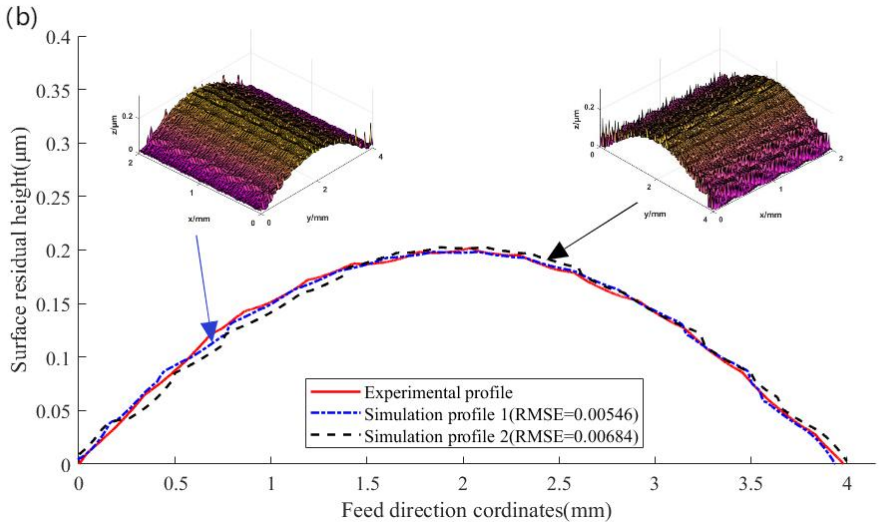

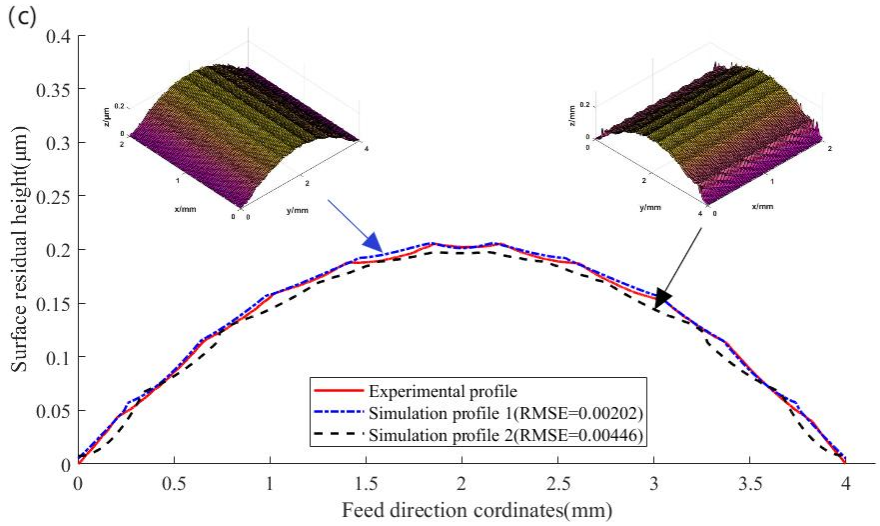

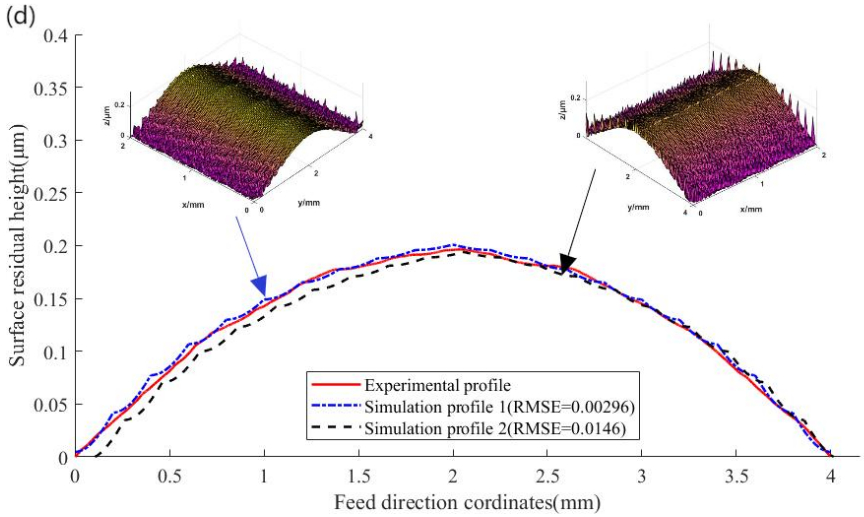

Figure 11. 2D profiles and 3D simulation diagrams under different parameters. Simulation profile 1 is the 2D contour line simulated using the improved Z-Map algorithm; Simulation profile 2 is the 2D contour line simulated using the traditional Z-Map algorithm.

The RMSE and MAPE values listed in Table 9 indicate relatively small deviations between simulation and experiment for both models. In particular, the improved Z-Map model yields lower error values, indicating improved agreement with experimental measurements and better surface representation capability.

Table 9. The RMSE and MAPE values under different conditions in Figure 11(a), (b), (c), and (d).

No.	Simulation profile 1		Simulation profile 2	
	RMSE	MAPE	RMSE	MAPE
Fig a	0. 0032	0. 0089	0. 0055	0. 0293
Fig b	0. 0055	0. 0121	0. 0068	0. 0342
Fig c	0. 0020	0. 0037	0. 0044	0. 0265
Fig d	0. 0030	0. 0045	0. 0146	0. 0568

5.2. Validation of the IBOA-RBFNN prediction model using experimental data

The IBOA-RBFNN model proposed in Section 3.1 was trained using 240 surface roughness samples generated from the improved Z-Map simulation (Section 4.2). The 16 experimental parameter combinations were not included in the training process, ensuring an independent dataset for model evaluation. To assess the generalization capability under real machining conditions, the process parameters (f_z, f_p, R, and η) from the 16 orthogonal experiments (Table 8) were input into the trained model, and the predicted surface roughness values were compared with experimental measurements obtained using a surface profilometer.

Figure 12 shows a comparison between experimental and predicted values across all 16 test cases. The predicted results generally follow the variation trend of the experimental measurements across the investigated parameter space. Quantitatively, the model achieves an MAE of 0.16 μm, an RMSE of 0.19 μm, an R^2 of 0.989, and a MAPE of 6.8%.

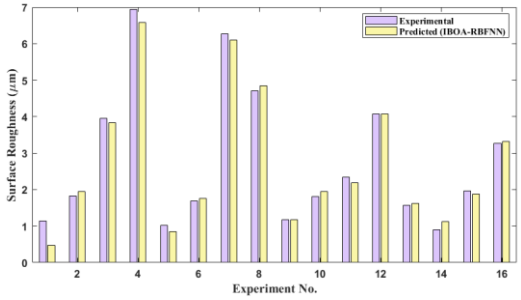

Figure 12. Comparison of experimental and IBOA-RBFNN predicted surface roughness for the 16 milling tests.

Compared with the simulation-based results reported in Section 4.2, the experimental validation shows increased prediction errors. This difference reflects the influence of practical machining uncertainties, such as tool wear, machine vibration, thermal effects, and material heterogeneity, which are not explicitly represented in the deterministic Z-Map simulation model.

The IBOA-RBFNN model still maintains reasonable agreement with experimental data, with a MAPE of 6.8%. This level of error is comparable to the deviation observed between the improved Z-Map simulation and experimental measurements reported in Section 4.1, indicating that the surrogate model preserves the predictive characteristics of the underlying simulation model. No significant overfitting

tendency is observed in the experimental validation results.

Therefore, the proposed model can serve as an efficient surrogate for surface topography prediction and provides a practical basis for subsequent reliability analysis.

5.3. Experimental verification of surface roughness reliability

Before presenting the reliability results, it is necessary to consider the influence of practical uncertainties such as machine tool vibrations, tool wear, and material inhomogeneity, which are not explicitly represented in deterministic geometric simulations. A reliability analysis based solely on idealized simulation data may therefore have limited direct interpretability for industrial applications.

As demonstrated in Section 5.2, the proposed IBOA-RBFNN surrogate model, although trained on noise-free simulation data, has been evaluated against experimental measurements. The model achieves satisfactory agreement with experimental results (MAE = 0.16 μm, MAPE = 6.8%), indicating that it is able to approximate the mapping between process parameters and surface roughness within the investigated machining conditions. This provides a reasonable basis for using the surrogate model as the evaluation function in the subsequent MC simulation.

Surface roughness reliability describes the probability that the surface quality remains within the specified tolerance limits during machining. Due to its direct influence on component performance, reliability evaluation is essential for quality control.

To validate the proposed reliability framework, machined specimens under different parameter settings were measured using the profilometer shown in Figure 9(a). Representative cases (Groups 3, 6, 11, and 12) illustrating the reliability evaluation procedure are presented in Figure 13. The full experiment was conducted across all 16 specimen groups. Each surface was divided into 350 overlapping 2 mm × 2 mm subregions. For each subregion, five repeated measurements were taken, and the mean of the three middle values was used as the representative surface roughness to reduce measurement noise. A subregion was classified as conforming if its surface roughness was within the specified allowable range, and reliability was defined as the proportion of conforming subregions.

Figure 13. Experimental procedure for roughness reliability evaluation: (a) Group 3, (b) Group 6, (c) Group 11, (d) Group 12.

Table 10. Surface roughness reliability values under different methods.

NO	Total number of measuring areas	Number of eligible areas	Reliability value			
			Experimental reliability value	IBOA-RBFNN-MC method	Response surface methodology	Monte Carlo method
1#	350	339	96. 9%	96. 41%	95. 13%	94. 56%
2#	350	340	97. 1%	97. 33%	97. 10%	96. 66%
3#	350	342	97. 7%	97. 54%	96. 82%	96. 96%
4#	350	338	96. 6%	96. 72%	95. 63%	95. 25%
5#	350	346	98. 9%	98. 46%	98. 12%	97. 35%
6#	350	335	95. 7%	95. 82%	94. 18%	95. 35%
7#	350	337	96. 3%	96. 54%	95. 77%	96. 21%
8#	350	345	98. 6%	98. 40%	97. 76%	96. 79%
9#	350	341	97. 4%	97. 32%	96. 14%	96. 27%
10#	350	331	94. 6%	94. 24%	93. 55%	94. 11%
11#	350	329	94. 0%	93. 74%	93. 16%	92. 78%
12#	350	343	98. 0%	98. 12%	97. 52%	97. 41%
13#	350	330	94. 3%	94. 15%	93. 88%	93. 57%
14#	350	336	96. 0%	95. 76%	95. 21%	94. 98%
15#	350	340	97. 1%	97. 23%	96. 67%	96. 56%
16#	350	343	98. 0%	97. 88%	97. 51%	97. 34%

Table 10 compares the reliability results obtained using the proposed IBOA-RBFNN-MC framework with experimental measurements. The predicted results show good agreement with experimental data and outperform conventional response surface and standard MC methods in terms of accuracy consistency.

A limitation of the current reliability analysis is the assumption that all input parameters follow independent normal distributions. Although this assumption is widely used in machining reliability studies due to its simplicity, it may not fully represent the statistical characteristics of real manufacturing processes [44].

In particular, non-Gaussian or correlated variations may affect the tail behavior of the response distribution, which directly influences failure probability estimation. Heavy-tailed distributions may increase the probability of extreme surface roughness values, while bounded distributions may lead to conservative estimates. Nevertheless, under the assumed probabilistic framework, the proposed IBOA-RBFNN-MC method provides a consistent and computationally efficient reliability evaluation approach. Future work will focus on incorporating non-Gaussian and correlated uncertainty models to improve the realism of reliability predictions.

6. Conclusion

This study presents an improved Z-Map milling surface topography simulation model, an IBOA-RBFNN-based surface roughness prediction model, and an IBOA-RBFNN-MC framework for surface roughness reliability analysis.

1) An improved Z-Map simulation framework was developed by embedding a PSO-based strategy into the nonlinear tool–surface intersection computation. Compared with conventional gradient-based solvers and existing Z-Map enhancement methods, the proposed derivative-free approach improves convergence stability in nonlinear tool–surface intersection computation, particularly in multi-solution regions. The model enables efficient simulation of milling surface topography under different combinations of fz, fp, R, and η, providing a computational basis for subsequent surface roughness prediction and reliability analysis.
2) An IBOA-optimized RBFNN surrogate framework is developed for surface roughness prediction and reliability analysis. The framework integrates chaotic initialization and an adaptive inertia weight mechanism to enhance the performance of the IBOA optimizer in balancing exploration and exploitation. Comparative results demonstrate improved prediction accuracy and more stable optimization behavior under the investigated conditions. Trained using noise-free PSO-enhanced Z-Map simulation data, the surrogate model provides an efficient mapping between machining parameters and surface roughness within the defined kinematic range, serving as the computational basis for subsequent reliability analysis.
3) To address uncertainties caused by process-parameter fluctuations during machining, the IBOA-RBFNN model is employed as a surrogate function and combined with the MC method to construct an IBOA-RBFNN-MC framework for surface roughness reliability analysis. Experimental comparisons indicate that the proposed framework shows better agreement with measured results than response-surface-based and conventional MC methods. This approach enables estimation of the probability that surface roughness exceeds the specified limits under process-parameter variations, providing a basis for surface quality evaluation under the investigated milling conditions.
4) The proposed framework is validated under a specific workpiece material, tool geometry, machining configuration, and parameter range. In addition, dynamic machining factors such as tool wear, cutting vibration, and thermal effects are not explicitly considered in the present model. The current analysis also assumes independent and normally distributed process parameters, which provides a practical approximation for reliability analysis but may not fully capture the actual statistical characteristics of manufacturing processes. Future work will extend the framework to broader machining conditions and incorporate dynamic effects as well as non-Gaussian and correlated uncertainty models to improve the robustness of surface-quality evaluation.

Acknowledgment

This research was supported by the National Natural Science Foundation of China (No. U24B2051, 52305261 and 51905334), the Academic Research Projects of Beijing Union University (No. ZK80202101 and ZK20202504), R & D Program of Beijing Municipal Education Commission (KM202211417012), Beijing Natural Science Foundation (L222111), and the Open Foundation of National Key Laboratory of Strength and Structural Integrity (ASSIKFJJ202305002).

References

1. Zhao B, Zhang S, Man J, Zhang Q, Chen Y. A modified normal contact stiffness model considering effect of surface topography. *Proceedings of the Institution of Mechanical Engineers, Part J: Journal of Engineering Tribology* 2015; 229(6): 677-688. https://doi.org/10.1177/1350650114558099.
2. Ait-Sadi H, Hemmouche L, Hattali L, Britah M, Lost A, Mesrati N. Effect of nanosilica additive particles on both friction and wear performance of mild steel/CuSn/SnBi multimaterial system. *Tribology International* 2015; 90: 372-385. https://doi.org/10.1016/j.triboint.2015.04.034.
3. Ghorbani M, Movahhedy M. Extraction of surface curvatures from tool path data and prediction of cutting forces in the finish milling of sculptured surfaces. *Journal of Manufacturing Processes* 2019; 45: 273-289. https://doi.org/10.1016/j.jmapro.2019.07.008.
4. Boz Y, Erdim H, Lazoglu I. A comparison of solid model and three-orthogonal dexelfield methods for cutter-workpiece engagement calculations in three- and five-axis virtual milling. *International Journal of Advanced Manufacturing Technology* 2015; 81(5-8): 811-823. https://doi.org/10.1007/s00170-015-7251-7.
5. Zhang W-H, Tan G, Wan M, Gao T, Bassir DH. A New Algorithm for the Numerical Simulation of Machined Surface Topography in Multiaxis Ball-End Milling. *Journal of Manufacturing Science and Engineering* 2008; 130(1): 011003-1-011003-11. https://doi.org/10.1115/1.2815337.
6. Chen H, Wang Q. Modelling and simulation of surface topography machined by peripheral milling considering tool radial runout and axial drift. *Proceedings of the Institution of Mechanical Engineers, Part B: Journal of Engineering Manufacture* 2019; 233(12): 2227-2240. https://doi.org/10.1177/0954405419838384.
7. Teimouri R, Grabowski M, Kowalczyk M, Skoczypiec S. Simulation of surface roughness alternation in milling-burnishing sequence. *Measurement* 2023; 218: 1-17. https://doi.org/10.1016/j.measurement.2023.113160.
8. Xu J, Zhang H, Sun Y. Swept surface-based approach to simulating surface topography in ball-end CNC milling. *International Journal of Advanced Manufacturing Technology* 2018; 98(1-4): 107-118. https://doi.org/10.1007/s00170-017-0322-1.
9. Li S, Dong Y, Li Y, Li P, Yang Z, Landers R. Geometrical simulation and analysis of ball-end milling surface topography. *International Journal of Advanced Manufacturing Technology* 2019; 102(5-8): 1885-1900. https://doi.org/10.1007/s00170-018-03217-5.
10. Xiao Y, Ge G, Zeng Z, Feng X, Du Z. An improved Z-MAP method based on the SQP algorithm for fast surface topography simulation of ball-end milling. *International Journal of Advanced Manufacturing Technology* 2023; 128(3-4): 1863-1878. https://doi.org/10.1007/s00170-023-11992-z.
11. Zekalmi Y, Albajez JA, Aguado S, Oliveros MJ. New fast micro-topography estimation algorithms for 5 axis milling. *Advances in Engineering Software* 2025; 205: 103909. https://doi.org/10.1016/j.advengsoft.2025.103909.
12. Guo Q, Liu Z, Jiang Y, Sun Y, Yang Z, Wang W, Zhao W, Okoye C. Topography prediction at boundaries between sub-regions in the 5-axis milling of Plexiglas based on dimension reduction method. *Journal of Manufacturing Processes* 2024; 131: 827-843. https://doi.org/10.1016/j.jmapro.2024.09.071.
13. Benardos P, Vosniakos G. Predicting surface roughness in machining: a review. *International Journal of Machine Tools & Manufacture* 2003; 43(8): 833-844. https://doi.org/10.1016/S0890-6955(03)00059-2.
14. Salgado D, Alonso F, Cambero I, Marcelo A. In-process surface roughness prediction system using cutting vibrations in turning. *International Journal of Advanced Manufacturing Technology* 2009; 43(1-2): 40-51. https://doi.org/10.1007/s00170-008-1698-8.
15. Duan C, Hao Q. Surface roughness prediction in high speed milling of 45 steel. *Journal of Harbin Engineering University* 2015; 36(9): 1229-1233. https://doi.org/10.11990/jheu.201412077. (In Chinese)

16. Zhao M, Xue B, Li B, Zhu J, Song W. Ensemble learning with support vector machines algorithm for surface roughness prediction in longitudinal vibratory ultrasound-assisted grinding. *Precision Engineering, Journal of the International Societies for Precision Engineering and Nanotechnology* 2024; 88: 382-400. https://doi.org/10.1016/j.precisioneng.2024.02.018.
17. Xu L, Huang C, Niu J, Wang J, Liu H, Wang X. Prediction of cutting power and surface quality, and optimization of cutting parameters using new inference system in high-speed milling process. *Advances in Manufacturing* 2021; 9(3): 388-402. https://doi.org/10.1007/s40436-020-00339-6.
18. Al-Ahmari A. Predictive machinability models for a selected hard material in turning operations. *Journal of Materials Processing Technology* 2007; 190(1-3): 305-311. https://doi.org/10.1016/j.jmatprotec.2007.02.031.
19. Zhang Y, Xiao G, Gao H, Zhu B, Huang Y, Li W. Roughness Prediction and Performance Analysis of Data-Driven Superalloy Belt Grinding. *Frontiers in Materials* 2022; 9: 765401. https://doi.org/10.3389/fmats.2022.765401.
20. Peng B, Yan X, Du J. Surface quality prediction based on BP and RBF neural networks. *Surface Technology* 2020; 49(10): 324- 328+337. https://doi.org/10.16490/j.cnki.issn.1001-3660.2020.10.038. (In Chinese)
21. Zhu Y, Meng F, Dai Y, Guo H, Shi C, Li Z. Prediction of Cutting Surface Roughness of Compacted Graphite Iron (CGI) Based on Machine Learning Techniques. *Iranian Journal of Science and Technology-Transactions of Mechanical Engineering* 2025; 49(4): 1765-1772. https://doi.org/10.1007/s40997-025-00869-z.
22. Zhan J, Zhou J, Xu Y, Chen J, Sun J. Research on ground surface roughness of cemented carbides with various grain sizes based on RBF neural network prediction. *Rare Metals and Cemented Carbides* 2022; 50(4): 87-93. https://doi.org/10.19990/j.issn.1004-0536.2022.04.087.07. (In Chinese)
23. Li J. Study of surrogate model approximation and surrogate-enhanced structural reliability analysis. PhD thesis. Shanghai: Shanghai Jiao Tong University; 2013. https://kns.cnki.net/kcms2/article/abstract?v=_Mh_dvKLMRvQTO53O-ot15hqtp8lv1RXPyJAvuDCh9wuJliWWM_kX4Z9gYHyanFCOUfd07B2ll_Zadq9CI5mz0NAV-pPHAXT0Ae5IBA8Mzx--GDJ0nKN39wkO8GIfSSigBEUIKM1SnnYLIDfUG2GQe_u1lAC0zOAc7cDD8Dg69W3Ech0YgNfv5cFDvxrkpvx&uniplatform=NZKPT&language=CHS. (In Chinese)
24. Deng J. Structural reliability analysis for implicit performance function using radial basis function network. *International Journal of Solids and Structures* 2006; 43(11-12): 3255-3291. https://doi.org/10.1016/j.ijsolstr.2005.05.055.
25. Wang Q, Fang H. Reliability analysis of tunnels using an adaptive RBF and a first-order reliability method. *Computers and Geotechnics* 2018; 98: 144-152. https://doi.org/10.1016/j.compgeo.2018.02.011.
26. Abbasianjahromi H, Shojaeikhah S. Structural Reliability Assessment of Steel Four-Bolt Unstiffened Extended End-Plate Connections Using Monte Carlo Simulation and Artificial Neural Networks. *Iranian Journal of Science and Technology-Transactions of Civil Engineering* 2021; 45(1): 111-123. https://doi.org/10.1007/s40996-020-00480-z.
27. Barbosa M, Rade D. Kriging/FORM Reliability Analysis of Rotor-Bearing Systems. *Journal of Vibration Engineering & Technologies* 2022; 10(6): 2179-2201. https://doi.org/10.1007/s42417-022-00511-1.
28. Luo C, Zhu SP, Keshtegar B, Macek W, Branco R, Meng D. Active Kriging-based conjugate first-order reliability method for highly efficient structural reliability analysis using resample strategy. *Computer Methods in Applied Mechanics and Engineering* 2024; 423: 116863. https://doi.org/10.1016/j.cma.2024.116863.
29. Ding F, Wang Q, Zhang L, Wang C. Support vector machine for hydraulic support reliability prediction. *Journal of Mechanical Strength* 2017; 39(3): 603-607. https://doi.org/10.16579/j.issn.1001.9669.2017.03.018. (In Chinese)
30. Chen JY, Feng YW, Teng D, Lu C, Fei CW. Support vector machine-based similarity selection method for structural transient reliability analysis. *Reliability Engineering & System Safety* 2022; 223: 108513. https://doi.org/10.1016/j.ress.2022.108513.
31. Schubert J. Managing inconsistent intelligence. In: *Proceedings of the Third International Conference on Information Fusion ; Paris, France. Piscataway, NJ: IEEE; 2000. p. TUB4/10-TUB4/16.* https://doi.org/10.1109/IFIC.2000.862669.
32. Smets P, Kennes R. The transferable belief model. *Artificial Intelligence* 1994; 66(2): 191-234. https://doi.org/10.1016/0004-3702(94)90026-4.
33. Jaberipour M, Khorram E, Karimi B. Particle swarm algorithm for solving systems of nonlinear equations. *Computers & Mathematics with Applications* 2011; 62(2): 566-576. https://doi.org/10.1016/j.camwa.2011.05.031.

34. Li F, Li Y, Li W, Wang B, Li Z. Surface roughness and surface morphology of milled carbon/epoxy composite surface. *Surface Technology* 2017; 46(9): 264-269. https://doi.org/10.16490/j.cnki.issn.1001-3660.2017.09.042. (In Chinese)
35. Arora S, Singh S. Butterfly optimization algorithm: a novel approach for global optimization. *Soft Computing* 2019; 23(3): 715-734. https://doi.org/10.1007/s00500-018-3102-4.
36. Liu J, Ma Y, Li Y. Improved butterfly algorithm for multi-dimensional complex function optimization problem. *Acta Electronica Sinica* 2021; 49(6): 1068-1076. https://doi.org/10.12263/DZXB.20200148. (In Chinese)
37. Gul N, Ahmed S, Elahi A, Kim S, Kim J. Optimal Cooperative Spectrum Sensing Based on Butterfly Optimization Algorithm. *Computers, Materials & Continua* 2022; 71(1): 369-387. https://doi.org/10.32604/cmc.2022.022260.
38. Tan L, Zainuddin Z, Ong P. Wavelet neural networks based solutions for elliptic partial differential equations with improved butterfly optimization algorithm training. *Applied Soft Computing* 2020; 95: 106518. https://doi.org/10.1016/j.asoc.2020.106518.
39. Sahoo AK, Panigrahi TK, Das SR, Behera A. Chaotic butterfly optimization algorithm applied to multi-objective economic and emission dispatch in modern power system. *Recent Advances in Computer Science and Communications* 2022; 15(2): 170-185. https://doi.org/10.2174/2666255813999200818140528.
40. Gotkhindikar NN, Singh M, Kataria R. Optimized deep neural network strategy for best parametric selection in fused deposition modelling. *International Journal on Interactive Design and Manufacturing* 2024; 18(8): 5865-5874. https://doi.org/10.1007/s12008-023-01369-7.
41. Jiang Z, Gu M. Optimization of a fender structure for the crashworthiness design. *Materials & Design* 2010; 31(3): 1085-1095. https://doi.org/10.1016/j.matdes.2009.09.047.
42. Freites A, Corbett P, Rongier G, Geiger S. Automated Classification of Well Test Responses in Naturally Fractured Reservoirs Using Unsupervised Machine Learning. *Transport in Porous Media* 2023; 147(3): 747-779. https://doi.org/10.1007/s11242-023-01929-1.
43. Al Debeyan F, Madeyski L, Hall T, Bowes D. The impact of hard and easy negative training data on vulnerability prediction performance. *Journal of Systems and Software* 2024; 211: 112003. https://doi.org/10.1016/j.jss.2024.112003.
44. Sekaninová M. Causes of Non-normality of Monitored Quality Characteristics in Process Capability Analysis. *Quality Innovation Prosperity* 2025; 29(3): 112-138. https://doi.org/10.12776/qip.v29i3.2266.